Automation in Construction 182 (2026) 106724

Contents lists available at ScienceDirect

Automation in Construction

journal homepage: www.elsevier.com/locate/autcon

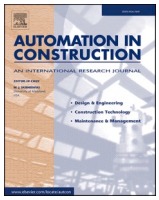

Scalable road infrastructure monitoring using embedded fiber Bragg grating sensors based on wavelet scattering-long short-term memory autoencoder

Ali Golmohammadi [a,*], Vahid Yaghoubi [b], Navid Hasheminejad [a], Nasser Ghaderi [c], Wim Van den bergh [a], David Hernando [a]

[a] SuPAR Research Group, Faculty of Applied Engineering, University of Antwerp, Antwerp, Belgium
[b] Q-VAIbe research group, Department of Aerospace Structures and Materials, Faculty of Aerospace Engineering, Delft University of Technology, Delft, Netherlands
[c] InViLab Research Group, University of Antwerp, Groenenborgerlaan 171, 2020 Antwerp, Belgium

ARTICLE INFO

Keywords:
Optical fiber sensor network
LSTM autoencoder
Health indicator
Intelligent health monitoring
Wavelet scattering network

ABSTRACT

Managing and extracting insights from the large volumes of data generated by optical fiber sensor networks is a major challenge. This paper presents an intelligent, scalable framework for real-time road health monitoring using fiber Bragg grating (FBG) sensor data. The proposed framework reduces reliance on manual data handling and cuts storage needs by over 99 % by constructing a compact health indicator (HI). Data preprocessing and fusion reduce volume and variability, while a wavelet scattering network (WSN) extracts damage-sensitive features that are encoded via a long short-term memory (LSTM) autoencoder to represent the health state. Temperature data is integrated to distinguish structural damage from environmental effects. The approach is evaluated through laboratory fatigue tests and synthetic damage data generated from healthy-state field measurements. Results demonstrate accurate, efficient monitoring with potential for edge deployment, enabling low-cost, real-time, long-term structural health management and representing a significant step toward automated, resource-efficient infrastructure maintenance.

1. Introduction

Various non-destructive testing (NDT) methods are widely used for road infrastructure monitoring [1], particularly in-situ sensing instruments and testing techniques that assess pavement condition and evaluate serviceability. However, conventional NDT approaches are typically periodic and require specialized equipment, trained personnel, and traffic closures, making them time-consuming and costly to deploy on a large scale. Furthermore, these methods operate offline, providing only snapshot assessments and limiting their ability to track the progression of structural damage over time. To address these limitations, an online monitoring strategy leveraging structural health monitoring (SHM) techniques is necessary. SHM is an interdisciplinary field focused on the continuous acquisition of data from various sensors integrated into infrastructure, aiming to identify potential structural deficiencies, monitor the condition of structures, and evaluate their safety. Research has shown that, in the early stages of SHM, changes in certain structural properties, such as stiffness, are often indicative of damage. By enabling early anomaly detection and facilitating timely interventions through structural repairs and disaster management, SHM enhances serviceability and extends the lifespan of civil infrastructure [2].

Different sensing methods, including vibration-based [3], acoustic-based [4], piezoelectric-based [5], and electrical resistance-based techniques [6] have been used for SHM purposes. The main limitation of conventional sensor technologies is the challenge of establishing a distributed sensing network. However, large-scale infrastructure, particularly roads, requires extensive monitoring for accurate assessment. Recently, optical fiber sensors have emerged as a promising solution for this purpose. These sensors offer both quasi-distributed sensing through fiber Bragg grating (FBG) technology [7] and fully distributed sensing using distributed optical fiber (DOF) sensors [8]. In addition to their sensing capabilities, due to their lightweight nature and resistance to electromagnetic interference, optical fiber sensors are well-suited for SHM applications [9].

However, while optical fiber sensors offer numerous capabilities, their deployment in large-scale networks generates vast amount of data

* Corresponding author.
E-mail address: seyedali.golmohammaditavalaei@uantwerpen.be (A. Golmohammadi).

https://doi.org/10.1016/j.autcon.2025.106724
Received 22 April 2025; Received in revised form 9 December 2025; Accepted 12 December 2025
Available online 18 December 2025

that cannot be efficiently processed using conventional analysis methods. A standard SHM workflow comprises three essential phases: collecting measurements, extracting features, and applying machine learning methods for feature classification [2]. However, this approach presents several challenges. First, extracting and formulating damage-sensitive features that remain robust against ambient temperature variations, noise, and other external factors is complex [2]. Additionally, implementing this protocol in a large sensor network with numerous sensors can be highly time-consuming. To address these limitations, deep learning has been proposed in several studies as a more efficient and effective tool for SHM [10].

The objective of this study is to develop an intelligent and scalable framework for automated health monitoring of road infrastructure using FBG sensor networks. The framework is designed and validated to integrate data management and pre-processing, feature extraction, and feature fusion modules that reduce data volume at multiple stages while preserving critical information and generating an interpretable health indicator (HI) that can detect damage and track structural degradation in real time. In addition, this study aims to account for environmental influences and the variability typical of real-field conditions by incorporating temperature data. Finally, the study seeks to quantify the framework's computational and storage efficiency to demonstrate its potential for edge analysis, as it minimizes the need to transfer and store large volumes of raw sensor data. Ultimately, it contributes to more efficient maintenance planning, reduced manual intervention, and enhanced long-term asset management.

The remainder of this paper is structured as follows. Section 2 reviews the related work on embedded sensing technologies, data-driven and AI-enhanced SHM approaches, and HI development for condition assessment. Section 3 presents the proposed intelligent SHM framework, including data management and pre-processing, feature extraction, feature fusion and model training, as well as HI construction. Section 4 describes the data collection process based on laboratory testing and field monitoring campaigns. Section 5 presents and discusses the implementation results of the proposed framework on the collected data and evaluates its computational efficiency and storage requirements. Finally, Section 6 concludes the paper, summarizes the main findings, and outlines future research directions.

2. Related work

This section reviews prior work on embedded sensing for SHM of pavements, highlighting current limitations in large-scale applications, followed by data-driven and AI-enhanced approaches and the data preparation required for these methods. It then examines existing research on HI construction and the metrics used to evaluate an optimal HI, which together form the methodological basis for the framework developed in this paper.

2.1. Embedded sensing and SHM for pavement

Advancements in SHM systems based on embedded sensing for road infrastructure have been explored from multiple perspectives to address the unique challenges of long-term pavement monitoring. These challenges stem from the need to monitor large-scale areas under variable environmental and loading conditions. A major area of focus in recent studies has been the identification of optimal sensors [11] or the development of new sensors [12] that meet the specific requirements of road infrastructure, particularly in terms of sensitivity and cost-efficiency. Since effective pavement monitoring often relies on deploying dense sensor networks across extended areas, the sensors must also be scalable and economically viable [13]. Parallel to sensor development, considerable effort has gone into improving sensor packaging to ensure durability under harsh roadway conditions [14]. These include repeated traffic loading, temperature fluctuations, moisture exposure, and chemical degradation. At the same time, packaging must allow for efficient strain transfer from the pavement structure to the sensor itself, which is critical for accurate measurement [15]. Another persistent challenge is ensuring a continuous power supply to embedded sensors, especially in large-scale installations. This limitation has driven interest in self-powered sensor solutions and energy harvesting technologies, which support autonomous operation without the need for extensive cabling or regular battery maintenance [16].

Despite these hardware-focused advancements, the efficient processing and interpretation of large volumes of sensor data remain a significant bottleneck in SHM systems for road infrastructure monitoring. As the size and resolution of sensor networks increase, so does the demand for intelligent frameworks that can automate feature extraction, reduce data dimensionality, and generate interpretable indicators of structural health. This need has led to a shift toward data-driven approaches that complement physical sensor design with machine learning and signal processing techniques. One of the critical challenges moving forward is the integration of data generated by smart pavements into existing pavement management systems (PMS) [17]. While some studies have proposed methods for incorporating sensor-based data into PMS, most current systems are not designed to handle the volume, complexity, and heterogeneity of data from advanced sensor networks. This highlights the urgent need for standardized protocols and interoperability guidelines to enable seamless data exchange and interpretation across various systems and regions. Without such standardization, large-scale adoption of smart pavement technologies may remain inefficient [18].

2.2. Data-driven, AI-enhanced approaches

With the rapid advancement of AI, interest in leveraging deep learning for SHM has grown significantly. Among various deep learning approaches, selecting an appropriate method remains a persistent challenge and should be carefully explored based on the specific requirements and characteristics of the available data and each application. For example, in most real-world applications, only unsupervised or semi-supervised techniques can work because labeled data is not available. Therefore, autoencoders can be a great option as they are unsupervised. In addition, they can effectively capture time dependencies. Therefore, this type of deep learning network has drawn attention recently in several studies. Moraes Coraça et al. [19] proposed a vibration-based SHM method that utilizes variational autoencoders combined with a hidden Markov model to evaluate structural deterioration using sensor data. Sarwar et al. [20] proposed a probabilistic temporal autoencoder for bridge SHM, effectively capturing features from multi-sensor data during train crossings. Li et al. [21] proposed an innovative "deploy-and-forget" SHM approach, integrating passive sensing, data compression techniques, and a mechanics-guided autoencoder to autonomously detect and localize structural damage. To detect structural damage and generate full-field data from limited inputs, Kulkarni et al. [22] developed a variational autoencoder informed by underlying physical models.

An important step in developing these types of models is data preparation, as using raw or partially pre-processed data can make the process highly time-consuming. Integrating signal processing, feature extraction, and multi-sensor data fusion at different levels [23] can greatly boost efficiency and optimize the overall performance of the process. One of the main focuses of this study is proper feature extraction for more accurate and time-efficient analysis. Conventional feature extraction methods, used to derive meaningful representations from raw data, comprise those from the frequency, time, and time-frequency domains. In the present study, a wavelet scattering network (WSN) [24] is utilized for feature extraction from signals. The scattering framework is designed to extract robust features that are resistant to shifts and distortions in input signals, which makes it especially effective for use in machine learning and deep learning contexts [25]. WSN shares several key attributes with deep learning architectures in terms of extracting

meaningful features from data [26]. However, a notable difference between wavelet scattering and deep learning methods is that the filters in scattering are predefined, rather than being learned during training. This distinction enables the scattering transform to be particularly advantageous in scenarios with limited training data, as it does not require the learning of filter responses [27].

2.3. Health indicator for condition assessment

Based on the previous discussion of data-driven and deep learning–based approaches for SHM, one advantage of these methods is that they can be employed to develop a HI for SHM. The health or damage condition of the monitored system is reflected by an HI, a particular feature obtained from SHM data [28]. HI can be an effective means for interpreting data and monitoring the structural condition over time, offering ongoing insights into its overall state throughout its service life. [29]. In certain industries, such as battery systems [30], rotating machinery [31], and composite structures [28], health management has received significant attention and has been implemented earlier. As a result, HIs are relatively well established in these fields. However, further research is needed to develop and refine HIs for applications in infrastructure monitoring. By defining a threshold for the HI based on required criteria, operators can make informed decisions regarding system maintenance [28]. Moreover, HIs may be utilized in predictive models to forecast a structure's remaining service life; however, this application falls outside the boundaries of the current study. Because damage evolves and accumulates in a nonlinear manner, HIs tend to display nonlinear patterns, which enhances their usefulness in examining and linking them to a structure's mechanical response [28]. However, HIs are not exclusively sensitive to damage; they may also be influenced by environmental conditions and operational variations [28]. Therefore, investigating methods to isolate the HI from environmental effects is essential for improving its reliability in damage assessment and ensuring its effectiveness in practical applications.

Numerous approaches and evaluation metrics have been introduced in previous research to establish an effective HI. In some studies, monotonicity, prognosability, and trendability are considered key metrics [32]. However, applying these metrics to data from in-situ civil structures is challenging, as their assessment typically requires multiple run-to-failure tests, which are often impractical. Other studies define general properties, including detectability (the degree of sensitivity of the HI to the existence of damage), separability (the ability of the HI to distinguish between damaged and healthy states), and trendability (the assumption that, following initial damage, the degradation pattern of the HI shows a positive correlation with the duration of operation) for an optimum HI [33]. Nevertheless, pinpointing the ideal HI that meets all three criteria is challenging. In practice, an HI can be regarded as optimal once it demonstrates both detectability and separability [33]. Therefore, this study adopted the second set of criteria, namely detectability, separability, and trendability, for HI development. In this study, detectability refers to the HI sensitivity to damage occurrence, separability indicates its ability to distinguish healthy from damaged states, and trendability describes its consistency in following damage progression over time.

3. Proposed methodology

This research proposes a framework for constructing HIs using an FBG sensor network embedded in road infrastructure. The framework, as illustrated in Fig. 1, begins with data acquisition, where multiple sets of FBG sensors embedded in the infrastructure continuously collect strain signals. Then, the raw sensor signals undergo data management and pre-processing steps to prepare the data for further analysis. Then, the signals are segmented, and features are extracted in the form of scattering coefficients at multiple levels using a WSN. The extracted features are then split into training, validation, and testing datasets. Here, the validation dataset is a subset of the training dataset used to monitor and prevent overfitting during the training process, while the remaining data, used as the test dataset, is later employed to evaluate the performance of the trained model in HI construction. For feature fusion, a long-short-term memory (LSTM) autoencoder is employed. The encoder part of the network captures temporal relationships within the data and transforms the features into a latent space representation. The trained encoder model for each dataset is subsequently used to process any newly arrived data from the monitoring system. Once new data is processed, the latent representations computed by the trained encoder model are used to construct HIs. These indicators are normalized and smoothed to ensure consistency. Finally, temperature measurements

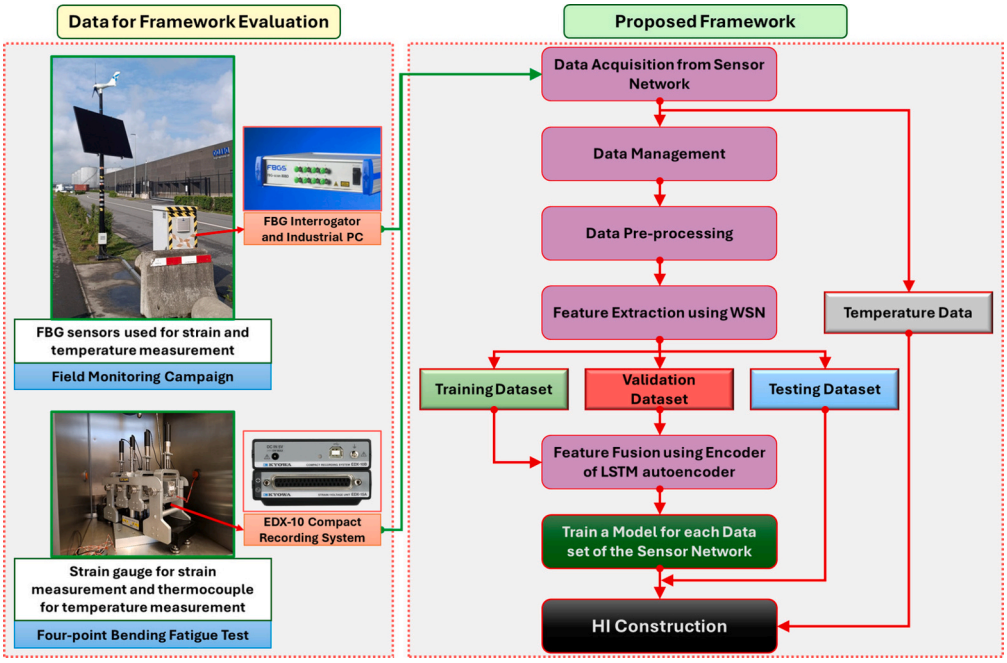

Fig. 1. Workflow for construction of health indicator (HI)

collected by the same FBG sensors during monitoring, serving as a baseline or ground truth, are integrated into the HI since strain data from damaged materials often deviate significantly from temperature-driven behaviour. Consequently, any substantial deviation of the HI from expected temperature variations provides a clear indication of damage initiation or progression in the monitored structure. This framework is finally evaluated using both a field monitoring campaign and a four-point bending fatigue test to ensure its validity under real-world and controlled conditions.

3.1. Data management and pre-processing

Before analyzing FBG sensor data, the data must be managed and pre-processed. A data management system for an FBG sensor network, recently proposed in [34], was used in this study to automatically manage data and remove measurement errors, thus improving accuracy in subsequent steps. Additionally, several methods for signal processing, such as filtering, thresholding, and concatenation, were applied to prepare long-term FBG data for analysis [34]. Filtering was performed using wavelet decomposition to remove signal baselines, specifically the low-frequency components induced by temperature variations (thermal strain), and retained only the high-frequency components caused by dynamic loading (mechanical strain). Thresholding was applied to retain only significant loading events, and finally, daily signals were concatenated to construct a long-term dataset (Fig. 2).

This pre-processing workflow was enhanced using multi-sensor data fusion at the data level to reduce variability in the measurements, following Eq. (1). As mentioned by Golmohammadi et al. [34], it is appropriate to fuse only the sensors positioned in the same transverse direction, as there is a time lag between sensors with a longitudinal offset. At each time step i, the fused data (F_{data}) can be obtained as follows:

$$F_{data}(i)=\begin{cases} FBG_1(i), if\,|FBG_1(i)|=max(|FBG_1(i)|,|FBG_2(i)|,\ldots,|FBG_k(i)|) \\ FBG_2(i), if\,|FBG_2(i)|=max(|FBG_1(i)|,|FBG_2(i)|,\ldots,|FBG_k(i)|) \\ \cdot \\ \cdot \\ \cdot \\ FBG_k(i), if\,|FBG_k(i)|=max(|FBG_1(i)|,|FBG_2(i)|,\ldots,|FBG_k(i)|) \end{cases} \tag{1}$$

Overall, these steps significantly reduced the size and variability of the dataset while retaining essential information, leading to improved computational efficiency for subsequent analysis.

3.2. Feature extraction using wavelet scattering network

Before training the deep learning model, efficient feature extraction is essential to reduce computational cost and training time. Without this step, using pre-processed raw data directly as model input would make the training process highly time-consuming and resource-intensive. This aligns with the data-centric AI approach, which emphasizes improving the quality and structure of data rather than increasing model complexity to enhance learning effectiveness [35]. Therefore, in this study, a WSN was applied to extract robust and compact features from the pre-processed and fused signals, making them suitable for input to the autoencoder. WSN is a method that can process time-related characteristics and multiple frequency components in a one-dimensional signal by capturing localized time-frequency information [36]. This approach is excellent for extracting precise and detailed characteristics because of its precise frequency and temporal resolution [37].

The wavelet scattering transform (WST) is an advanced technique for time-frequency analysis, capable of effectively extracting low-frequency features while preserving high-frequency details. Compared to the conventional wavelet transform, it provides additional advantages such as translation invariance and stability to small deformations [38]. The WST procedure generally involves three primary stages: convolution, application of a nonlinear operation, and averaging. The following steps outline the WST computation:

1) The complex wavelet transform can be expressed as:

$$x*\psi_\lambda(t)=x*\psi_\lambda^a(t)+jx*\psi_\lambda^b(t) \tag{2}$$

2) The wavelet mode coefficients are calculated using the following expression:

$$U[\lambda]x=|x*\psi_\lambda(t)| \tag{3}$$

The nonlinear operation, which is known as the modulus operation, is performed as follows:

$$|x*\psi_\lambda(t)|=\sqrt{|x*\psi_\lambda^a(t)|^2+|x*\psi_\lambda^b(t)|^2} \tag{4}$$

3) Convolutional averaging with the scaling function is represented by the following formula:

$$S[\lambda]x=|x*\psi_\lambda(t)|*\phi(u) \tag{5}$$

Here, the original signal is represented by $x(t)$, the scaling function $\phi(t)$, and the complex wavelet basis by $\psi_\lambda(t)$. In terms of capturing global features across time, the WST mentioned above overcomes the drawbacks of the conventional wavelet transform. It offers stability to local deformations, retains rich feature information, and avoids amplifying noise present in the original signal [39]. In this framework, a WSN is constructed, in which the WST is repeatedly applied, following a hierarchical structure, as illustrated in Fig. 3.

As shown in Fig. 3, the initial network layer processes the input signal $x(t)$ to generate the scattering coefficient S_0. The resulting mode coefficients U_1 are then passed to the next layer, which produces the scattering coefficients S_1. This process continues as the mode coefficients U_2 are fed into the subsequent network layer, repeating the cycle. Fig. 4 illustrates the schematic of the WSN, with its detailed formulation provided below:

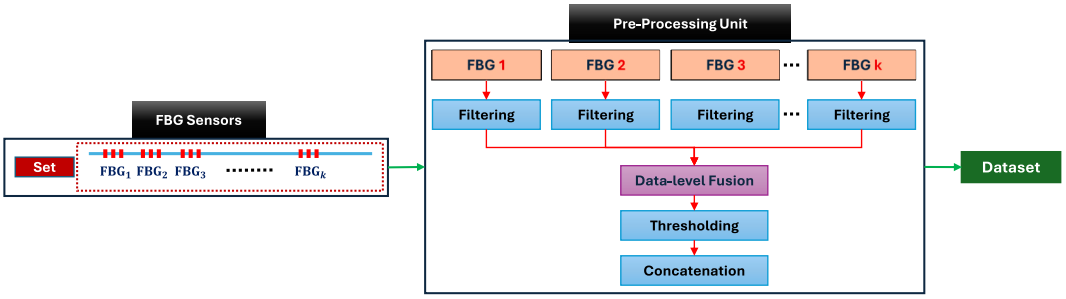

Fig. 2. General steps for pre-processing and data fusion of the FBG sensor network.

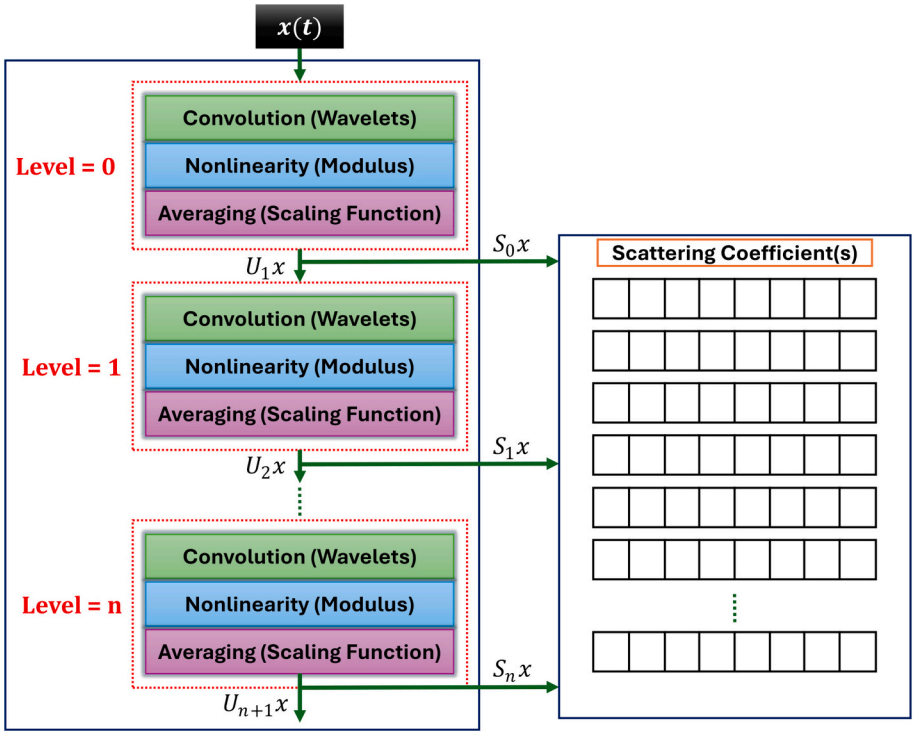

Fig. 3. Hierarchical architecture of the wavelet scattering network (WSN).

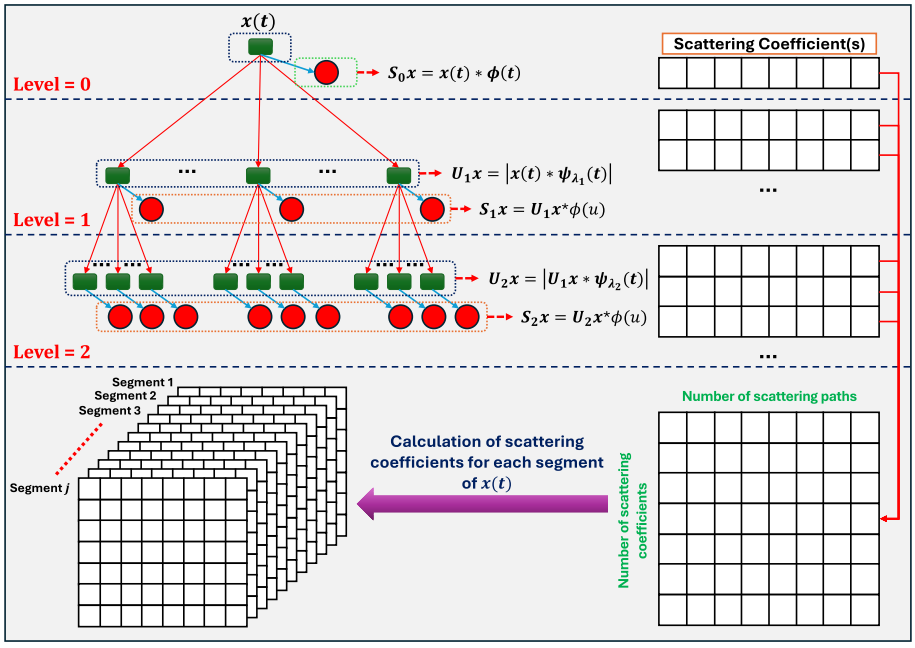

Fig. 4. Schematic of feature extraction from sensor data using wavelet scattering networks

1) This is the representation of the wavelet scattering coefficient at level 0:

$$S_0x = x^*\phi(u) \tag{6}$$

2) The initial signal x is convolved with $\psi_\lambda(t)$, and the extracted modes are represented as $U_1x = |x^*\psi_{\lambda_1}(t)|$. This result is then used as input to level 1, where it is convolved with $\phi(t)$ to compute the following:

$$S_1x = U_1x^*\phi(u) \tag{7}$$

3) At level 2, U_2x and at level 3,S_2x can be calculated as:

$$U_2x = ||x^*\psi_{\lambda_1}(t)|^*\psi_{\lambda_2}(t)| = |U_1x^*\psi_{\lambda_2}(t)| \tag{8}$$

$$S_2x = ||x^*\psi_{\lambda_1}(t)|^*\psi_{\lambda_2}(t)|^*\phi(u) = U_2x^*\phi(u) \tag{9}$$

4) By iteratively progressing through each layer, the n-th layer is computed as follows:

$$U_n x = |||x * \psi_{\lambda_1}(t)| * \psi_{\lambda_2}(t)| \ldots * \psi_{\lambda_n}(t)| = |U_{n-1} x * \psi_{\lambda_n}(t)| \quad (10)$$

$$S_n x = |||x * \psi_{\lambda_1}(t)| * \psi_{\lambda_2}(t)| \ldots * \psi_{\lambda_n}(t)| * \phi(u) = U_n x * \phi(u) \quad (11)$$

To summarize, the propagation operator computes the total scattering path $p = (\lambda_1, \lambda_2, \ldots, \lambda_n)$, producing a set of wavelet scattering coefficients denoted as $\{S_1, S_2, S_3, \ldots, S_n\}$, which are considered the extracted features from the input signal [39]. In this study, only the mechanical strain component of the data, obtained after removing thermal strain, was used as input to the WSN.

3.3. Feature fusion and model training using LSTM autoencoder

After feature extraction using WSN, the next step is feature fusion, which transforms high-dimensional wavelet scattering coefficients into low-dimensional representations suitable for health monitoring. These representations capture key temporal patterns in the data while significantly reducing data volume and computational overhead, forming the basis for HI construction in the subsequent step.

In this study, an LSTM autoencoder was utilized for this purpose. The LSTM architecture was specifically chosen because it is particularly well-suited for processing sequential data by accurately modeling temporal relationships and identifying long-range patterns [40]. Generally, an autoencoder is designed to replicate its input data and comprises the encoder and the decoder as its two main parts. The LSTM autoencoder was trained to reconstruct the scattering features; after training, only the encoder was used to generate latent features for health indicator construction. During training, the encoder learns a set of compact features, referred to as the latent representation, which captures essential patterns and structures from the input data [41]. The latent representation is critical as it encapsulates the most significant features of the input data, enabling tasks such as anomaly detection. In this study, scattering coefficients served as the input data for the encoder. Finally, the trained model can be applied to process new data from the monitoring system, generating latent representations. This model is illustrated in Fig. 5.

A two-layer bidirectional LSTM (bi-LSTM) network was utilized within the encoder to combine the extracted features into compact latent representations. Unlike standard LSTMs, a bi-LSTM processes sequences in both forward and backward directions and includes key components such as a memory cell (g), an input (i), an output (o), and a forget (f) gates. This architecture is specifically designed to retain long-range dependencies in sequential data through its internal memory structure [28,42]. As depicted in Fig. 5, the current input (x_t), along with the previous hidden (h_{t-1}) and cell (c_{t-1}) states, contribute to updating the hidden state (h_t) at time step t^{th}, ensuring past information is retained. The process follows these equations [28,42]:

$$f_t = \sigma\left(W_f x_t + U_f h_{t-1} + b_f\right) \quad (12)$$

$$i_t = \sigma\left(W_i x_t + U_i h_{t-1} + b_i\right) \quad (13)$$

$$g_t = tanh\left(W_g x_t + U_g h_{t-1} + b_g\right) \quad (14)$$

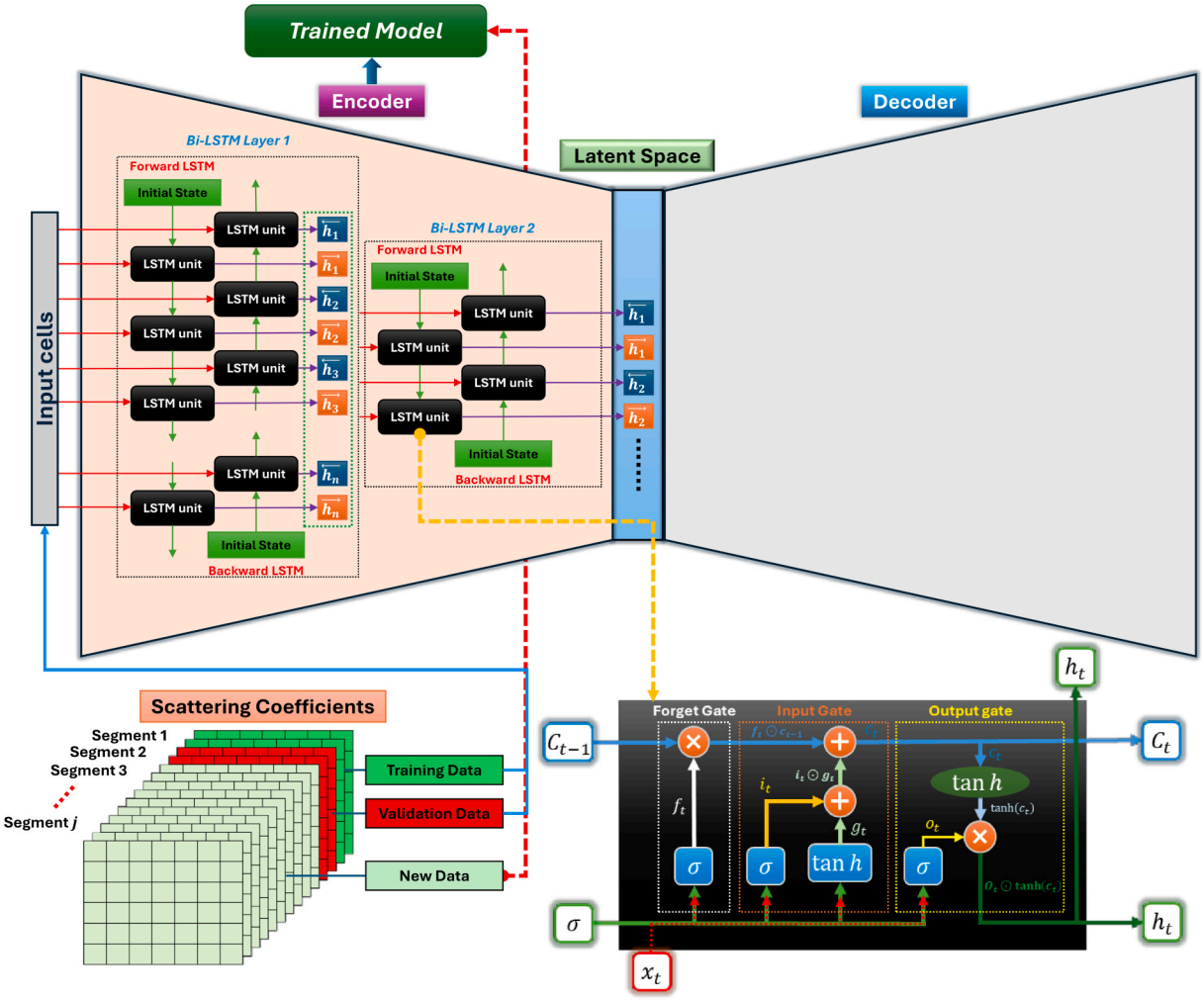

Fig. 5. Architecture of LSTM autoencoder for feature fusion and model training (only the encoder is used during inference).

$$o_t = \sigma(W_o x_t + U_o h_{t-1} + b_o) \tag{15}$$

$$c_t = f_t \odot c_{t-1} + i_t \odot g_t \tag{16}$$

$$h_t = o_t \odot tanh(c_t) \tag{17}$$

Here, σ denotes the sigmoid activation function, *tanh* is the hyperbolic tangent function, and $\odot$ represents element-wise multiplication. Trainable weight metrics, W_* and U_*, are associated with the present input and the preceding hidden state, respectively, while b_* represents the corresponding trainable bias parameters for each gate. Unlike standard LSTM, bi-LSTMs process input sequences bidirectionally, enabling them to capture dependencies in both historical and prospective situations [43].

3.4. Construction of health indicator

This study defines HI as a single scalar value that represents the structural condition of the pavement over its lifetime, summarizing deviations from a healthy baseline. The healthy baseline represents the undamaged condition of the structure and is established using the training and validation data collected under normal operational and environmental conditions before any damage is introduced. In the proposed framework, the HI is derived from this healthy baseline. The trained model produces multiple forward–backward latent pairs for each segment. The latent variables corresponding to the healthy baseline are represented as follows:

$$\mathrm{h}_{base} = \left[\overrightarrow{h}_1, \overrightarrow{h}_2, \ldots, \overrightarrow{h}_M, \overleftarrow{h}_1, \overleftarrow{h}_2, \ldots, \overleftarrow{h}_M\right] \tag{18}$$

where M is the number of latent pairs, which depends on the number of LSTM units defined in the encoder's hidden layer configuration. For each new data segment, the trained model generates a corresponding vector of latent variables expressed as:

$$\mathrm{h}_{j,\mathrm{new}} = \left[\overrightarrow{h}_{1,\mathrm{new}}(j), \overrightarrow{h}_{2,\mathrm{new}}(j), \ldots, \overrightarrow{h}_{M,\mathrm{new}}(j), \overleftarrow{h}_{1,\mathrm{new}}(j), \overleftarrow{h}_{2,\mathrm{new}}(j), \ldots, \overleftarrow{h}_{M,\mathrm{new}}(j)\right] \tag{19}$$

where j is the segment index. When new data arrive from the sensors, the model generates these latent variables as outputs for each segment. However, since these latent variables are inherently noisy, a smoothing process is applied to enhance clarity. To ensure meaningful comparisons, the absolute values of these latent variables are calculated (since they may contain negative values), followed by normalization using the z-score relative to the training and validation datasets. Formally, the HI for segment j is defined as:

$$HI(j) = \max_{i=1,\ldots,M} \left\{ \frac{\left|\overrightarrow{h}_{i,\mathrm{new}}(j)\right| - \mu_{\overrightarrow{h}_i}}{\sigma_{\overrightarrow{h}_i}}, \frac{\left|\overleftarrow{h}_{i,\mathrm{new}}(j)\right| - \mu_{\overleftarrow{h}_i}}{\sigma_{\overleftarrow{h}_i}} \right\} \tag{20}$$

Here, $\overrightarrow{h}_i$ and $\overleftarrow{h}_i$ denote the forward and backward latent variables from the healthy baseline, respectively, while $\mu_{\overrightarrow{h}_i}$, $\mu_{\overleftarrow{h}_i}$ and $\sigma_{\overrightarrow{h}_i}$, $\sigma_{\overleftarrow{h}_i}$ represent the mean and standard deviation of their absolute values computed from the healthy baseline. Finally, for simplicity, only the latent variable with the maximum deviation is selected to serve as the HI for each dataset (Fig. 6).

In addition, according to Eq. (21), the strain measured by FBG sensors ($\varepsilon_{measured}$) is a combination of mechanical strain ($\varepsilon_{mechanical}$) and thermal strain ($\varepsilon_{thermal}$) [44]. After pre-processing FBG data based on Section 3.1, the thermal strain is removed, leaving only the mechanical strain. However, as shown in Eq. (22), even after removing the thermal strain, the remaining mechanical strain is still indirectly influenced by temperature (T) as modulus (E) is a function of T. In real field applications, since information about loading (σ) and loading frequency (f) is typically unavailable, temperature is the only measurable factor. Therefore, tracking temperature data alongside the constructed HIs as ground truth can help distinguish whether variations in HI result from environmental temperature changes or actual structural damage.

$$\varepsilon_{measured} = \varepsilon_{mechanical} + \varepsilon_{thermal} \tag{21}$$

$$\varepsilon_{mechanical} = \frac{\sigma}{E(T,f)} \tag{22}$$

Finally, the monitored temperature data needs to be smoothed and normalized relative to the temperature recorded for the training and validation datasets as ground truth. This guarantees that the effects of temperature changes on the HI can be distinguished from possible signs of damage. Fig. 6 illustrates this process for the construction of HIs.

4. Measurements

This section presents two complementary measurement campaigns used to evaluate the proposed health monitoring framework. The first campaign involves a laboratory-based four-point bending fatigue test, enabling stress-controlled loading and progressive damage development in a specimen instrumented with strain gauge (SG) sensors. The second campaign describes a real-world field monitoring system using embedded FBG sensors in a road test track.

4.1. Four-point bending fatigue test

An experimental test was designed to obtain strain data under conditions that closely resemble real-field scenarios. To achieve this, a thermal chamber-equipped dynamic testing apparatus was employed to conduct a four-point bending fatigue test under stress-controlled conditions at 10 Hz. Also, the temperature was randomly varied during the test to simulate real environmental effects.

For this test, a beam specimen was fabricated with dimensions of 60 × 60 × 400 mm. A groove was created at the center of the bottom face of the beam to accommodate SG sensors and wiring, ensuring proper installation without interfering with the test rig supports (Fig. 7a). Subsequently, three foil SGs with a 10 mm gauge length and one with a 20 mm gauge length were glued on the central third of the beam as

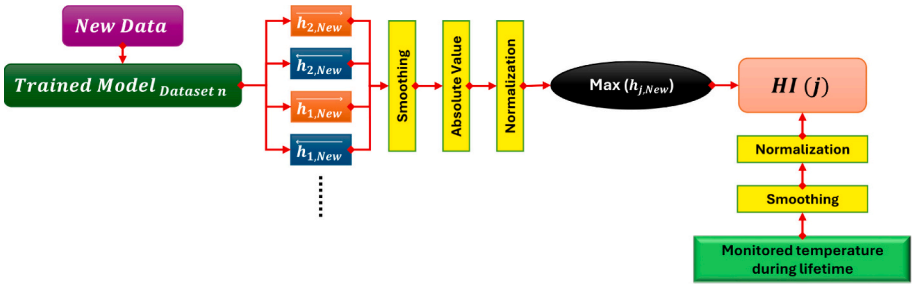

Fig. 6. Process of HI construction using the trained model

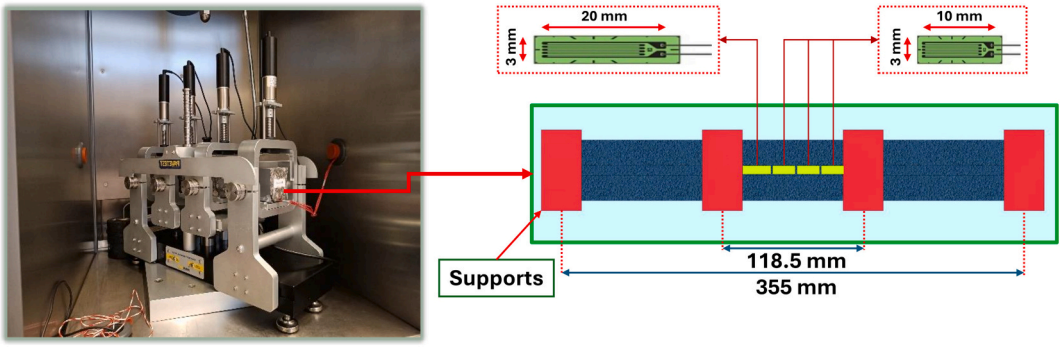

Fig. 7. Experimental setup for fatigue test.

depicted in Fig. 7b. Foil strain gauges were used only in this test, as it was destructive and FBG sensors were not a cost-effective option for such conditions.

The DCS-100 A software was used to process the strain data that was gathered throughout the test using a recording device (EDX-10) with a sampling frequency of 500 Hz. Additionally, the specimen temperature was recorded throughout the test using a thermocouple (Fig. 8a). During the fatigue test time, damage initiated and progressed in the specimen, eventually leading to failure. This damage occurred at the second sensor location, as shown in Fig. 8b.

Fig. 9a–d illustrate the responses of all sensors during the test. As observed, since the damage occurred at the SG2 location, its strain response exhibited an increasing trend, indicating damage propagation. In contrast, the other sensors do not show a clear trend, as their variations were primarily attributed to temperature fluctuations. Additionally, a decrease in strain amplitude was observed in these sensors. At the beginning of the test, when the sample was still in a healthy state, all SGs displayed nearly identical responses.

This experiment demonstrates that the proximity of a sensor to the damage location determines the reaction of a deployed sensor network in the presence of damage. This issue is particularly important in quasi-distributed sensor networks (such as FBG sensor networks) compared to fully distributed sensor networks (such as DOF sensor networks), as the former covers a smaller area, increasing the risk of damage occurring in regions without sensing points. Therefore, the development of a technique capable of capturing damage both within the sensing region and its vicinity is crucial for achieving more reliable structural health monitoring.

4.2. *Field monitoring campaign*

An embedded FBG sensor network was used to perform additional measurements on a field road test track at the Port of Antwerp-Bruges [34,45,46]. In this test track, the FBG sensor network was embedded during construction in four different layers and two sections to monitor strain in both lateral and longitudinal directions, with the configuration shown in Fig. 10. Additionally, the temperature in each layer was also monitored using FBG sensors. Within each optical fiber, a specific sensor was calibrated exclusively for temperature measurement, enabling the measurement of the actual pavement temperature. A continuous monitoring campaign was carried out from April 28, 2024, to October 17, 2024, with a sampling frequency of 100 Hz, utilizing an FBG-Scan 708D optical interrogator with eight channels. Since the road was newly constructed, no signs of damage were present in the data. Therefore, all field measurements correspond to healthy-state pavement conditions. Moreover, as analyzing all sensors in the network is unnecessary at this stage, a limited number of FBG sensors were selected for analysis (Fig. 10).

Fig. 11a presents an example of FBG data for a single day, along with long-term pre-processed and fused FBG data (Fig. 11b), and temperature collected over the monitoring campaign duration (Fig. 11c).

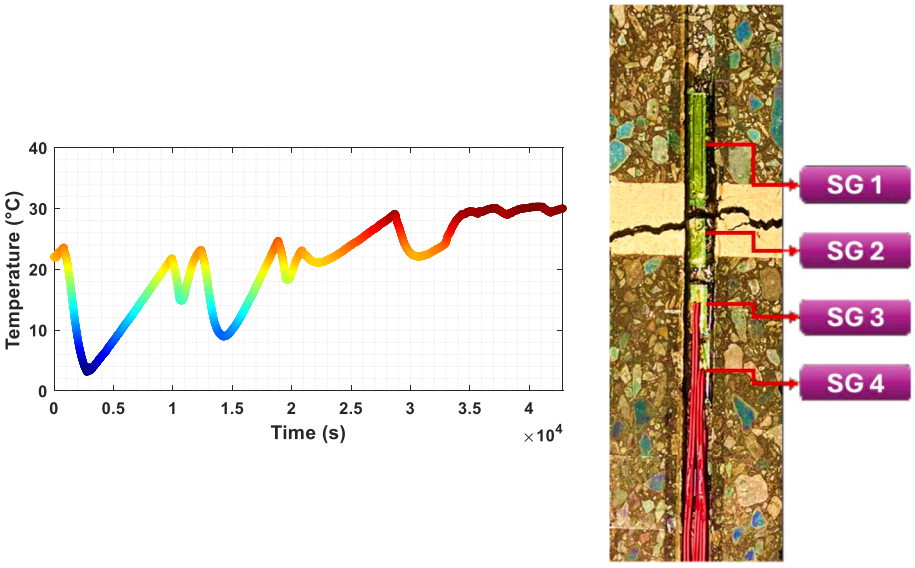

Fig. 8. Experimental test: (a) Temperature during test, (b) damage and strain gauge sensor location

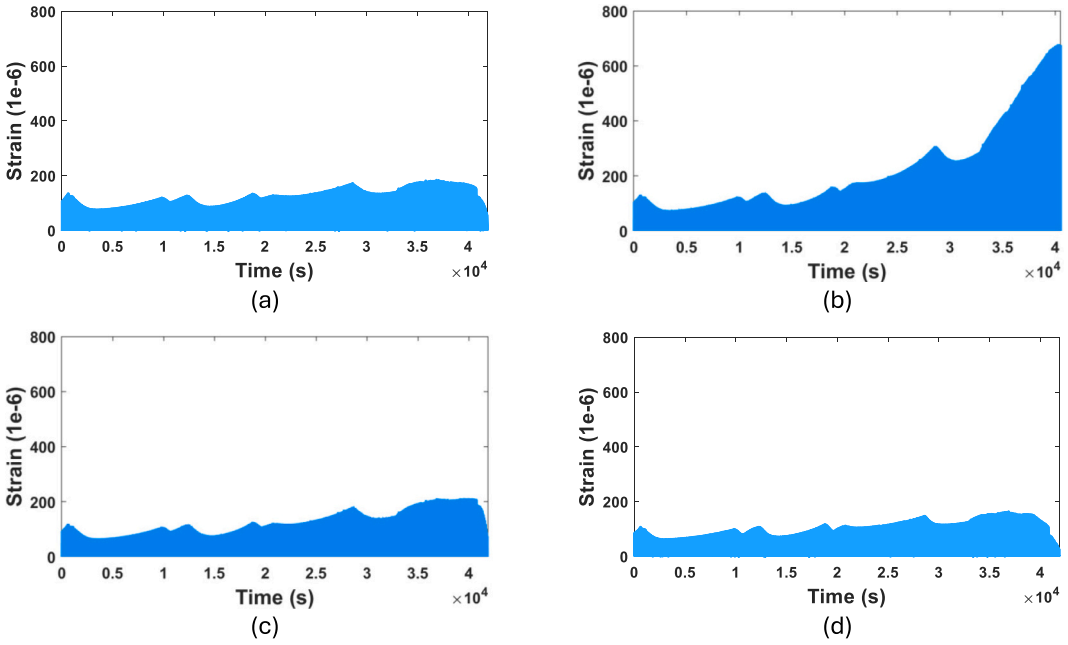

Fig. 9. Responses from strain gauge sensors: (a) SG1, (b) SG2, (c) SG3, and (d) SG4.

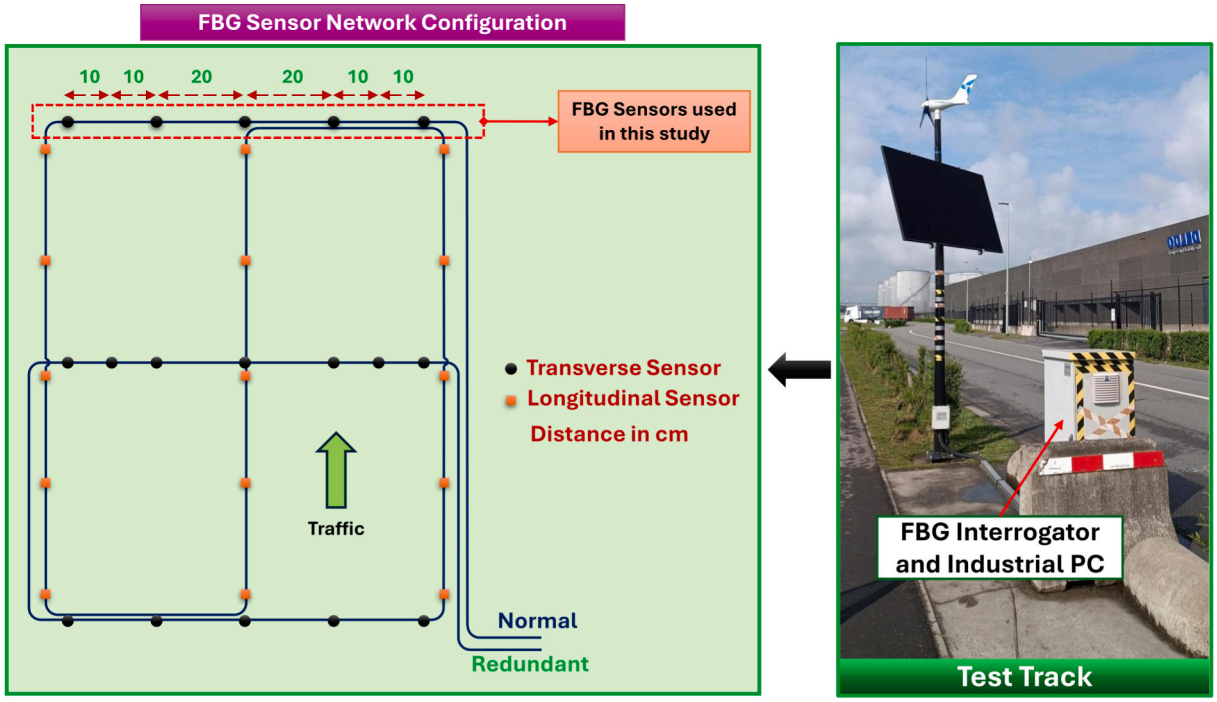

Fig. 10. Road monitoring system using embedded FBG sensor network.

5. Results and discussion

This section implements the proposed framework on both experimental and field-acquired FBG sensor network data to evaluate its practical relevance and performance in real-world conditions. Then, the results were analyzed and discussed in detail.

5.1. Implementation in experimental laboratory data

The implementation of the proposed framework in experimental laboratory data begins with feature extraction, as the data was already pre-processed using the DCS-100 A software. Since four SGs were mounted on the sample, there is no need for data fusion, as the objective is to observe the effect of damage on all sensors individually, and there are no limitations on data storage.

First, each SG signal was divided into three datasets: training (5000 s), validation (5000 s), and testing (the remaining signal). For feature extraction using a WSN, the SG signals were segmented into 500-data-point windows. Since the sampling frequency was 500 Hz, each segment represents one second of data. Fig. 12 illustrates examples of the scattering coefficients for different segments of the SG3 signal.

After extracting the features (scattering coefficients) of each

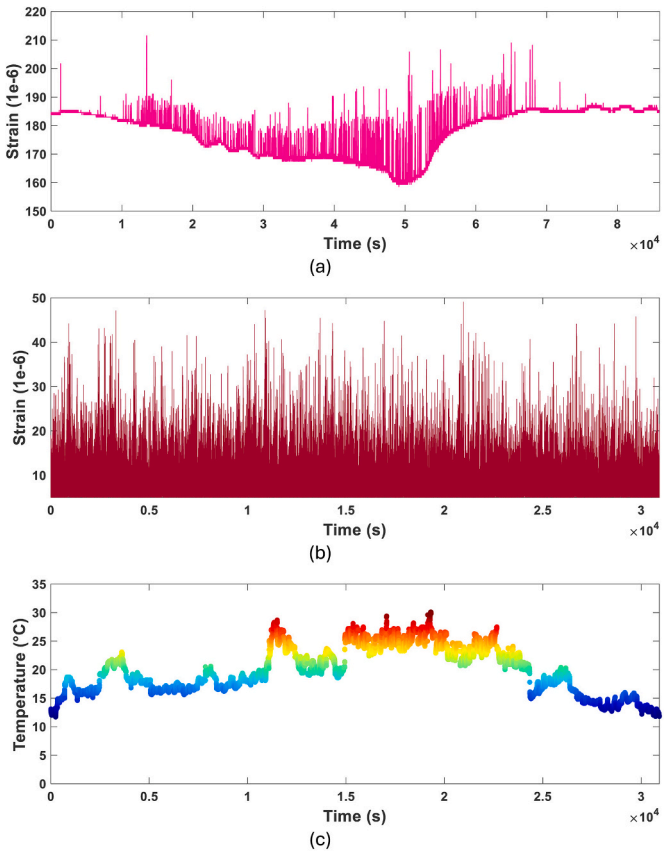

Fig. 11. Example of FBG sensor data: (a) One-day raw data from sensor 30 on 20/06/2024, (b) long-term pre-processed and fused data for selected sensors over the monitoring campaign duration, (c) temperature data collected throughout the monitoring campaign.

segment, they were used as input for an LSTM autoencoder to train the encoder. The hidden layer of the encoder was designed with 128 Bi-LSTM units, enabling the network to efficiently learn and represent intricate temporal relationships within the data. The second layer contains 2 Bi-LSTM units, which compress the extracted features into a low-dimensional latent representation. These values can be optimized based on specific requirements, though optimization is beyond the scope of this study. After training the models, the constructed HI for each SG can be seen in Fig. 13.

As shown in Fig. 13, the HIs constructed following the proposed method align with temperature variations during the structure's healthy phase. Once damage begins to occur, the HI for SG2 began a progressive trend and noticeably deviated from the temperature variation, with this deviation intensifying as the damage progressed toward the failure point.

In contrast, the HIs for the other SGs exhibited a minor increase and deviation from temperature, as illustrated in Fig. 13. This deviation could have been more pronounced if additional data were available beyond the failure point.

5.2. Implementation on field FBG sensor network data

The proposed framework for constructing the HI was applied to real field data from an FBG sensor network. Unlike the experimental laboratory data, the field data were collected under real traffic conditions, making it essential to verify that the proposed method remained effective in this scenario. Since the road is currently in a healthy state with no visible damage, the available data were considered as the baseline (healthy state). To evaluate the framework's response to potential damage, synthetic damage data $\varepsilon_d(t)$ were generated from the healthy-state field measurements by applying an exponential scaling function $f(t)$ to the healthy strain signal $\varepsilon_h(t)$:

$$\varepsilon_d(t) = f(t)\,\varepsilon_h(t) \tag{23}$$

where $f(t)$ defines the progressive change in strain amplitude due to damage. In the first scenario (S1), damage led to an exponential increase in strain level amplitude informed by laboratory fatigue test results (section 4.1). The second scenario (S2) was included to account for other potential damage mechanisms, which may result in an exponential decrease in strain level amplitude. These effects were modeled using $f(t)$ of the form:

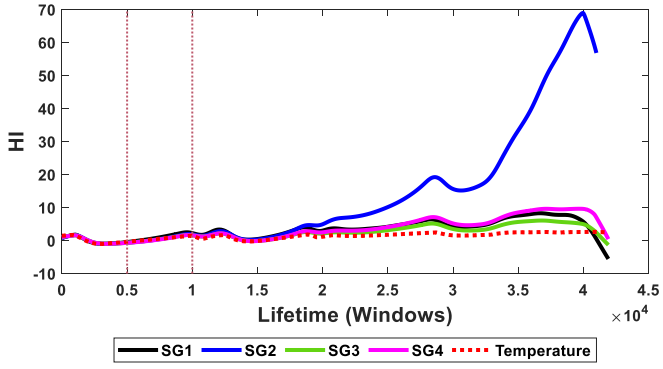

Fig. 13. Health indicator (HI) constructed for each SG signal.

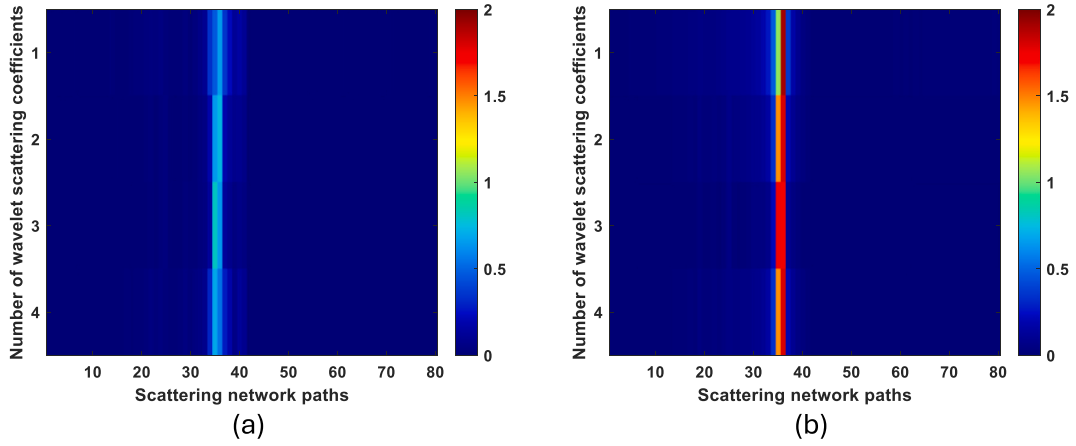

Fig. 12. Example of the scattering coefficient for SG3: (a) Segment 50 from the training dataset, (b) Segment 29,000 from the test dataset.

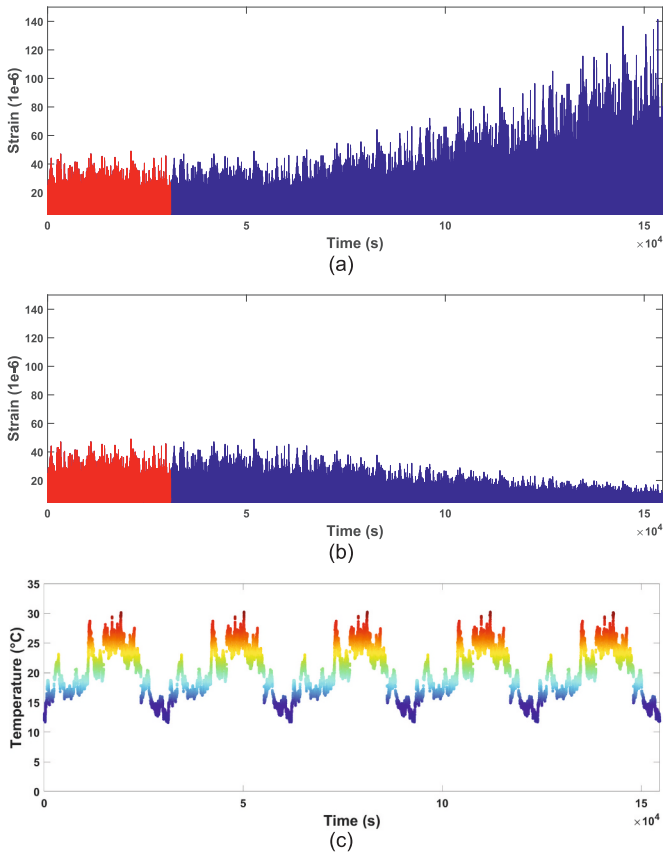

Fig. 14. Synthetic data generated from real FBG sensor data: (a) S1 ($t_0 =$ 60,000 and $\tau = max(t)/2$), (b) S2, (c) Temperature.

$$f(t) = \begin{cases} 1, t \le t_0 \\ 1 + \left(e^{\pm(t-t_0)/\tau} - 1\right), t > t_0 \end{cases} \quad (24)$$

where t_0 is the delay before the damage effect becomes noticeable, and τ is the time constant that controls the rate of exponential growth (positive sign) or decay (negative sign). This formulation ensures a smooth transition from the undamaged baseline to the altered strain level, reflecting the progressive nature of structural degradation. A simple baseline correction was then applied to remove slow drifts while preserving the original dynamic signal characteristics. These two scenarios are illustrated in Fig. 14a-b. Additionally, since temperature data were only available for the healthy state, it was assumed that this temperature pattern repeated over time, as shown in Fig. 14c.

These data served as input for the proposed framework, where the FBG data were divided into three datasets: training (5000 s), validation (5000 s), and testing (remaining signal). For feature extraction using a WSN, the FBG signals were segmented into 500-data-point windows. Given the sampling frequency of 100 Hz, each segment corresponds to 5 s of data. Fig. 15 shows an example of the scattering coefficients for various segments of the S1 scenario.

After feature extraction, the same LSTM autoencoder was used to train and encode the data. The results of the constructed HI for the S1 and S2 scenarios are shown in Fig. 16.

The HIs for both scenarios exhibit a progressive trend as damage is initiated, confirming the practicality and performance of the proposed framework in real-world applications. As expected, both signals closely followed the temperature variation in the healthy state. However, with the onset of damage, they began to deviate from the temperature trend, serving as an indicator of damage severity.

These HIs can be constructed in the same way for a large number of FBG sensor data points within a network. They can then be straightforwardly tracked in a single graph. The next step after constructing the HI would be to define a threshold that serves as a criterion for identifying the end of life. This threshold can be either fixed or adaptive, depending on the HI trend or its deviation relative to temperature variations. Determining an appropriate threshold is crucial not only for damage identification but also for estimating the remaining useful life (RUL).

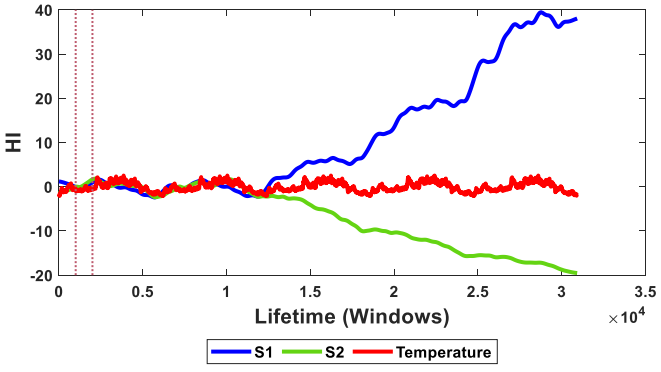

Fig. 16. Health indicator (HI) constructed for S1 and S2 scenarios.

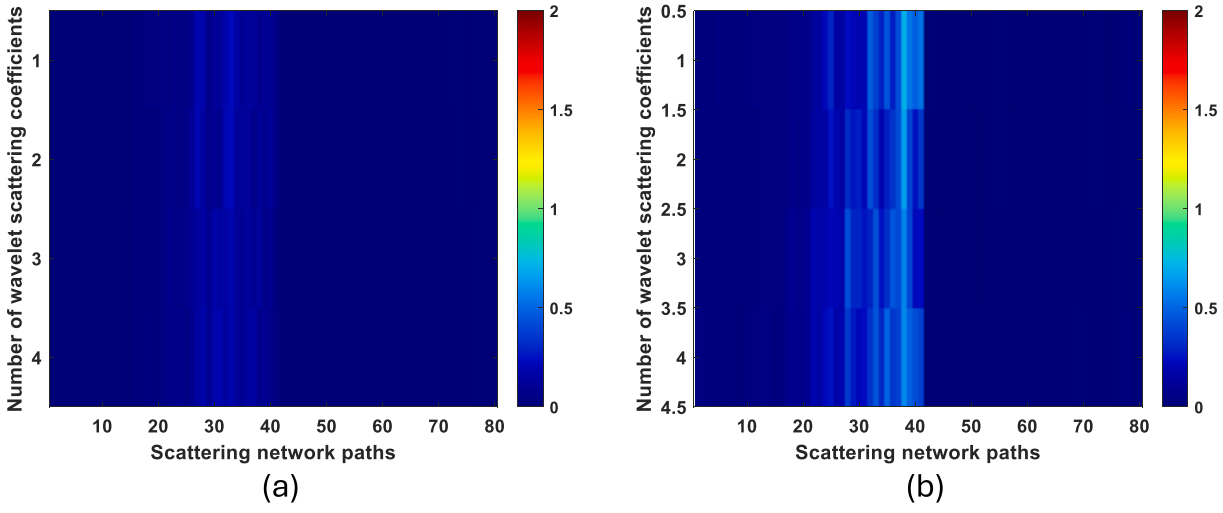

Fig. 15. Example of the scattering coefficient for the S1 scenario: (a) Segment 100 from the training dataset, (b) Segment 20,000 from the test dataset.

5.3. Computational efficiency and storage requirements

During the field monitoring campaign, a total of 156 sensors were operational across the network, producing approximately 20 GB of raw data per day. In the current workflow, these data are compressed to about 2 % of their original size before transmission to a network-attached storage (NAS) unit, and then decompressed for offline analysis. This process adds significant computational time (about 30 min per day) and storage overhead. This highlights the need for lightweight frameworks capable of performing edge analysis, thereby eliminating the need for full data transmission and storage.

In contrast, the proposed framework in this study reduces raw data from gigabytes to only kilobytes per HI, achieving over 99 % reduction in data volume. These HIs can be transmitted almost instantly to a central server, avoiding the delays and costs associated with full-scale data handling. Such improvements demonstrate substantial potential for reducing processing time, memory requirements, and operational costs in future large-scale pavement monitoring systems.

The training and testing processes were conducted in MATLAB on a laptop equipped with an NVIDIA GeForce RTX 4080 Laptop GPU (12.88 GB), an Intel Core i9-13900H CPU (2.60 GHz), and 64 GB of RAM. For the experimental strain gauge data, training the LSTM autoencoder took approximately 18–19 min per sensor. Once trained, inference was performed with an average processing time of approximately 0.6–0.9 milliseconds per segment. For the field FBG data, training required around 11–12 min, and inference on test segments took an average of approximately 0.5–0.7 milliseconds per segment. This lightweight computational demand confirms that the framework is suitable for on-device or edge implementation in field-deployable SHM systems, where rapid, low-resource processing is essential.

6. Conclusions

This paper proposed a framework for intelligent health monitoring of road infrastructure using FBG sensor networks embedded in pavement layers. The framework consists of four main units: data collection and pre-processing, feature extraction, feature fusion, and HI construction. It was evaluated using both experimental laboratory data and synthetic damage data generated from the healthy-state field measurements. The framework introduces a fully automated pipeline, directly contributing to automation in construction by reducing the need for manual intervention, improving real-time monitoring, and enabling data-driven decision-making. Based on the analyses and results obtained, the following conclusions were drawn:

- Sensor response is influenced by its distance from the damage location. Therefore, an optimal HI should be sensitive to cases where the damage is either at the sensor location or in its vicinity.
- The WSN can automatically extract damage-sensitive features, improving computational efficiency compared to using raw data directly as encoder input, which is computationally expensive.
- Features can be fused and compressed into a latent space using the encoder component of an LSTM autoencoder during inference, eliminating the need for the decoder at deployment. This reduces computational time and memory requirements.
- A model trained on healthy-state data can be used for health monitoring of newly arriving data. Based on the fusion plan, each dataset yields a single HI value per window of events (each event corresponds to a vehicle pass), eliminating the need to store large volumes of raw data.
- Incorporating temperature data alongside the HI improves its reliability and interpretability by enabling the distinction between variations caused by environmental conditions and those resulting from structural damage, facilitating early damage detection.
- The proposed HI exhibits key characteristics of an optimal HI, including detectability and separability. However, when the damage is located in the sensor's neighbourhood, trendability is not fully achieved.
- Using experimental and synthetic data, the results suggest that the proposed framework successfully identifies and tracks the onset and progression of damage under the tested conditions.

This study highlights the transformative potential of intelligent, data-driven frameworks in road infrastructure monitoring. By compressing vast sensor datasets into real-time, interpretable HIs, such approaches can shift pavement management strategies from reactive maintenance to proactive, cost-efficient asset preservation. Beyond pavements, the methodology could be adapted to other transportation infrastructures such as bridges, tunnels, and rail networks, and is adaptable to other strain-sensing technologies. If widely adopted, this type of framework could significantly enhance how agencies prioritise interventions and allocate public funds for infrastructure maintenance.

Despite promising results, several limitations remain. First, reliance on synthetic damage data for part of the evaluation limits the direct evidence of performance under real degradation scenarios. Second, the feasibility of edge deployment was conceptually shown but not physically tested on embedded hardware. These limitations directly motivate the following research directions.

Future work should address these limitations through large-scale field evaluations under real degradation events, full hardware-in-the-loop testing for edge computing deployment, and integration with existing PMS. Extending the framework to enable accurate RUL estimation would further strengthen predictive maintenance capabilities and support long-term infrastructure management. In the long term, frameworks of this kind have the potential to form the backbone of fully autonomous, self-monitoring infrastructure networks, minimising maintenance costs, maximising service life, and enhancing public safety.

Declaration of generative AI and AI-assisted technologies in the writing process

During the preparation of this work the author(s) used ChatGPT to assist with grammar improvement. After using this tool, the author(s) reviewed and edited the content as needed and take(s) full responsibility for the content of the published article.

CRediT authorship contribution statement

Ali Golmohammadi: Writing – original draft, Visualization, Validation, Software, Methodology, Formal analysis, Conceptualization. **Vahid Yaghoubi:** Writing – review & editing, Methodology, Investigation, Conceptualization. **Navid Hasheminejad:** Writing – review & editing, Supervision, Investigation, Conceptualization. **Nasser Ghaderi:** Writing – review & editing, Investigation. **Wim Van den bergh:** Resources, Project administration, Investigation, Funding acquisition. **David Hernando:** Writing – review & editing, Validation, Supervision, Investigation.

Declaration of competing interest

The authors declare the following financial interests/personal relationships which may be considered as potential competing interests: (Wim Van den bergh reports financial support was provided by Port of Antwerp-Bruges. If there are other authors, they declare that they have no known competing financial interests or personal relationships that could have appeared to influence the work reported in this paper.)

Acknowledgment

This study was funded by the Port of Antwerp-Bruges under project 48231, "*Durable Pavements for Port Area – Heavily Loaded Pavements: Exploration and In-depth Study*." The authors also thank Com&Sens for

their valuable technical support during the sensor installation and data collection phases. Additionally, the authors gratefully acknowledge the support of the Research Foundation – Flanders (FWO) for funding the research stay that contributed to this work (Grant No. V463524N).

Data availability

The authors do not have permission to share data.

References

[1] D.M. Barbieri, B. Lou, Instrumentation and testing for road condition monitoring–a state-of-the-art review, NDT E Int. (2024) 103161, https://doi.org/10.1016/j.ndteint.2024.103161.
[2] Y.-J. Cha, R. Ali, J. Lewis, O. Büyüköztürk, Deep learning-based structural health monitoring, Autom. Constr. 161 (2024) 105328, https://doi.org/10.1016/j.autcon.2024.105328.
[3] R. Bajwa, E. Coleri, R. Rajagopal, P. Varaiya, C. Flores, Pavement performance assessment using a cost-effective wireless accelerometer system, Comput. Aided Civ. Inf. Eng. 35 (1009–1022) (2020) 1009–1022, https://doi.org/10.1111/mice.12544.
[4] M.R. Ganji, A. Ghelmani, A. Golroo, H. Sheikhzadeh, Asphalt pavement macrotexture monitoring in cracked surfaces by using an acoustical low-cost continuous method, Autom. Constr. 132 (2021) 103932, https://doi.org/10.1016/j.autcon.2021.103932.
[5] F. Gulisano, T. Buasiri, F.R.A. Apaza, A. Cwirzen, J. Gallego, Piezoresistive behavior of electric arc furnace slag and graphene nanoplatelets asphalt mixtures for self-sensing pavements, Autom. Constr. 142 (2022) 104534, https://doi.org/10.1016/j.autcon.2022.104534.
[6] D. Han, G. Liu, Y. Xi, X. Xia, Y. Zhao, Real-time monitoring of strain and modulus of asphalt pavement using built-in strain sensor cluster, Constr. Build. Mater. 384 (2023) 131413, https://doi.org/10.1016/j.conbuildmat.2023.131413.
[7] H.-P. Wang, Y.-B. Wu, C. Zhang, P. Xiang, Monitoring data motivated health condition assessment of cement concrete pavements in field based on FBG sensing technology, Struct. Health Monit. (2024), https://doi.org/10.1177/14759217241268821, 14759217241268820.
[8] M. Zeng, H. Chen, J. Ling, H. Zhao, D. Wu, Monitoring of prestressing forces in cross-tensioned concrete pavements during construction and maintenance based on distributed optical fiber sensing, Autom. Constr. 142 (2022) 104526, https://doi.org/10.1016/J.AUTCON.2022.104526.
[9] B. Chen, Z. Zhu, Z. Su, W. Yao, S. Zheng, P. Wang, Optical fiber sensors in infrastructure monitoring: a comprehensive review, Intell. Transport. Infrastruct. 2 (2023) liad018, https://doi.org/10.1093/iti/liad018.
[10] L. Zheng, J. Xiao, Y. Wang, W. Wu, Z. Chen, D. Yuan, W. Jiang, Deep learning-based intelligent detection of pavement distress, Autom. Constr. 168 (2024) 105772, https://doi.org/10.1016/j.autcon.2024.105772.
[11] Z. Liu, B. Cui, Q. Yang, X. Gu, Sensor-based structural health monitoring of asphalt pavements with semi-rigid bases combining accelerated pavement testing and a falling weight deflectometer test, Sensors 24 (2024) 994, https://doi.org/10.3390/s24030994.
[12] T. Ma, N. Wang, C. Han, S. Wang, Z. Tong, Asphalt pavement residual life assessment based on SmartRock sensors, IEEE Trans. Instrum. Meas. 72 (2023) 1–12, https://doi.org/10.1109/TIM.2023.3267372.
[13] A. Di Graziano, V. Marchetta, S. Cafiso, Structural health monitoring of asphalt pavements using smart sensor networks: a comprehensive review, J. Traffic Transport. Engineer. (Engl. Ed.) 7 (2020) 639–651, https://doi.org/10.1016/j.jtte.2020.08.001.
[14] Y. Liu, J. Xie, S. Liu, Y. Zhao, Y. Zhu, G. Qi, Research on the methodology of development and calibration of flexible encapsulated fiber Bragg grating sensors, Measurement 201 (2022) 111730, https://doi.org/10.1016/j.measurement.2022.111730.
[15] H. Wang, P. Xiang, L. Jiang, Strain transfer theory of industrialized optical fiber-based sensors in civil engineering: a review on measurement accuracy, design and calibration, Sens. Actuat. A Phys. 285 (2019) 414–426, https://doi.org/10.1016/j.sna.2018.11.019.
[16] H.B. Birgin, E. García-Macías, A. D'Alessandro, F. Ubertini, Self-powered weigh-in-motion system combining vibration energy harvesting and self-sensing composite pavements, Constr. Build. Mater. 369 (2023) 130538, https://doi.org/10.1016/j.conbuildmat.2023.130538.
[17] S. Abejide, M.M.H. Mostafa, D. Das, B. Awuzie, M. Rahman, Pavement quality index rating strategy using fracture energy analysis for implementing smart road infrastructure, Sensors 21 (2021) 4231, https://doi.org/10.1016/j.conbuildmat.2023.130538.
[18] A.K.M. Hossein, A. Golroo, M. Akhoundzadeh, Smart embedded technologies and materials for enhanced pavement management, Autom. Constr. 168 (2024) 105865, https://doi.org/10.1016/j.autcon.2024.105865.
[19] E.M. Coraça, J.V. Ferreira, E.G.O. Nóbrega, An unsupervised structural health monitoring framework based on Variational autoencoders and hidden Markov models, Reliab. Eng. Syst. Saf. 231 (2023) 109025, https://doi.org/10.1016/j.ress.2022.109025.
[20] M.Z. Sarwar, D. Cantero, Probabilistic autoencoder-based bridge damage assessment using train-induced responses, Mech. Syst. Signal Process. 208 (2024) 111046, https://doi.org/10.1016/j.ymssp.2023.111046.
[21] X. Li, H. Bolandi, M. Masmoudi, T. Salem, A. Jha, N. Lajnef, V.N. Boddeti, Mechanics-informed autoencoder enables automated detection and localization of unforeseen structural damage, Nat. Commun. 15 (2024) 9229, https://doi.org/10.1038/s41467-024-52501-4.
[22] N.N. Kulkarni, A. Sabato, Full-field expansion and damage detection from sparse measurements using physics-informed variational autoencoders, Struct. Health Monit. (2024), https://doi.org/10.1177/14759217241289575, 14759217241289576.
[23] S. Hassani, U. Dackermann, M. Mousavi, J. Li, A systematic review of data fusion techniques for optimized structural health monitoring, Inf. Fusion 103 (2024) 102136, https://doi.org/10.1016/j.inffus.2023.102136.
[24] J. Andén, S. Mallat, Deep scattering spectrum, IEEE Trans. Signal Process. 62 (2014) 4114–4128, https://doi.org/10.1109/TSP.2014.2326991.
[25] Y. Chen, T. Xu, T. Xu, Intelligent non-cooperative optical networks: leveraging scattering neural networks with small training data, Opt. Commun. 560 (2024) 130465, https://doi.org/10.1016/j.optcom.2024.130465.
[26] S. Mallat, Understanding deep convolutional networks, Philos. Trans. R. Soc. A Math. Phys. Eng. Sci. 374 (2016) 20150203, https://doi.org/10.1098/rsta.2015.0203.
[27] Z. Baharlouei, H. Rabbani, G. Plonka, Wavelet scattering transform application in classification of retinal abnormalities using OCT images, Sci. Rep. 13 (2023) 19013, https://doi.org/10.1038/s41598-023-46200-1.
[28] M. Moradi, A. Broer, J. Chiachío, R. Benedictus, T.H. Loutas, D. Zarouchas, Intelligent health indicator construction for prognostics of composite structures utilizing a semi-supervised deep neural network and SHM data, Eng. Appl. Artif. Intell. 117 (2023) 105502, https://doi.org/10.1016/j.engappai.2022.105502.
[29] C. Song, K. Liu, X. Zhang, Integration of data-level fusion model and kernel methods for degradation modeling and prognostic analysis, IEEE Trans. Reliab. 67 (2017) 640–650, https://doi.org/10.1109/TR.2017.2715180.
[30] Y. Ma, C. Shan, J. Gao, H. Chen, Multiple health indicators fusion-based health prognostic for lithium-ion battery using transfer learning and hybrid deep learning method, Reliab. Eng. Syst. Saf. 229 (2023) 108818, https://doi.org/10.1016/j.ress.2022.108818.
[31] T. Yan, X. Xing, D. Wang, K.-L. Tsui, M. Xia, Interpretable degradation tensor modeling through multi-scale and multi-level time-frequency feature fusion for machine health monitoring, Inf. Fusion 117 (2025) 102935, https://doi.org/10.1016/j.inffus.2025.102935.
[32] J. Coble, J.W. Hines, Identifying optimal prognostic parameters from data: a genetic algorithms approach, in: Annual Conference of the PHM Society 1, 2009. No. 1.
[33] H. Zhou, X. Huang, G. Wen, Z. Lei, S. Dong, P. Zhang, X. Chen, Construction of health indicators for condition monitoring of rotating machinery: a review of the research, Expert Syst. Appl. 203 (2022) 117297, https://doi.org/10.1016/j.eswa.2022.117297.
[34] A. Golmohammadi, D. Hernando, N. Hasheminejad, Advanced data-driven FBG sensor-based pavement monitoring system using multi-sensor data fusion and an unsupervised learning approach, Measurement 242 (2025) 115821, https://doi.org/10.1016/j.measurement.2024.115821.
[35] P. Singh, Systematic review of data-centric approaches in artificial intelligence and machine learning, Data Sci. Manag. 6 (2023) 144–157, https://doi.org/10.1016/j.dsm.2023.06.001.
[36] S. Jayalakshmy, J.K. Pragatheeswaran, D. Saraswathi, N. Poonguzhali, Scattering convolutional network based predictive model for cognitive activity of brain using empirical wavelet decomposition, Biomed. Signal Process Control. 66 (2021) 102501, https://doi.org/10.1016/j.bspc.2021.102501.
[37] F. Wang, D. Chen, W. Yao, R. Fu, Real driving environment EEG-based detection of driving fatigue using the wavelet scattering network, J. Neurosci. Methods 400 (2023) 109983, https://doi.org/10.1016/j.jneumeth.2023.109983.
[38] A. Patwa, M.M.U. Rahman, T.Y. AI-Naffouri, Heart murmur and abnormal PCG detection via wavelet scattering transform & a 1D-CNN, IEEE Sensors J. (2025), https://doi.org/10.1109/JSEN.2025.3541320.
[39] H. Liu, N. Wang, H. Fang, X. Yu, W. Du, Identification of the number of leaks in water supply pipes based on wavelet scattering network and Bi-LSTM model with Bayesian optimization, Measurement 243 (2025) 116348, https://doi.org/10.1016/j.measurement.2024.116348.
[40] S. Hochreiter, J. Schmidhuber, Long term short memory, Neural Comput. 9 (1997) 1735–1780, https://doi.org/10.1162/neco.1997.9.8.1735.
[41] D. Bank, N. Koenigstein, R. Giryes, Autoencoders, Machine Learning for Data Science Handbook: Data Mining and Knowledge Discovery Handbook, 2023, pp. 353–374, https://doi.org/10.1007/978-3-031-24628-9.
[42] F. Liang, L. Duan, W. Ma, Y. Qiao, J. Miao, Q. Ye, Context-aware network for RGB-D salient object detection, Pattern Recogn. 111 (2021) 107630, https://doi.org/10.1016/j.patcog.2020.107630.

[43] A. Graves, S. Fernández, J. Schmidhuber, Bidirectional LSTM networks for improved phoneme classification and recognition, in: International Conference on Artificial Neural Networks, Springer, 2005, pp. 799–804, https://doi.org/10.1007/11550907_126.
[44] FBG Total Strain Thermal Considerations | Five Steps to Meaningful Strain Data Technical Note 1025, Micron Optics, Inc, Luna Inc., 2014. Revision 2014.06.17) 4–4. TN 1025 - Total Strain.pdf, https://lunainc.com/sites/default/files/assets/files/resource-library/TN%201025%20-%20Total%20Strain.pdf.
[45] A. Golmohammadi, N. Hasheminejad, D. Hernando, An innovative data analysis approach via peak-counting–based segmentation for pavement monitoring using FBG sensors, J. Test. Eval. 53 (2025), https://doi.org/10.1520/JTE20240123.
[46] D. Hernando, S.A.G. Tavalaei, N. Hasheminejad, W. Van Den Bergh, E. Voet, Exploring the use of fiber Bragg grating sensors for monitoring the structural response of asphalt pavements, in: Bituminous Mixtures and Pavements VIII, CRC Press, 2024, pp. 708–716. ISBN: 978–1–032-51494-9 (hbk), 978–1–032-51497-0 (pbk), 978–1–003-40254-1 (ebk), https://doi.org/10.1201/9781003402541-83.